

Received April 5, 2019, accepted June 9, 2019, date of publication June 24, 2019, date of current version July 31, 2019. Digital Object Identifier 10.1109/ACCESS.2019.2924713

# Leveraging Gaussian Process Regression and Many-Objective Optimization Through Voting Scores for Fault Identification

PEI CAO<sup>®</sup>1, (Student Member, IEEE), QI SHUAI<sup>2</sup>, AND JIONG TANG<sup>®</sup>1, (Member, IEEE)

<sup>1</sup>Department of Mechanical Engineering, University of Connecticut, Storrs, CT 06269, USA

<sup>2</sup>School of Automotive Engineering, Chongqing University, Chongqing 400044, China

Corresponding author: Jiong Tang (jiong.tang@uconn.edu)

This work was supported by the National Science Foundation under Grant CMMI - 1825324.

**ABSTRACT** Using piezoelectric impedance/admittance sensing for structural health monitoring is promising, owing to the simplicity in circuitry design as well as the high-frequency interrogation capability. The actual identification of fault location and severity using impedance/admittance measurements, nevertheless, remains to be an extremely challenging task. A first-principle-based structural model using finite element discretization requires high dimensionality to characterize the high-frequency response. As such, direct inversion using the sensitivity matrix usually yields an under-determined problem. Alternatively, the identification problem may be cast into an optimization framework, in which the fault parameters are identified through the repeated forward finite element analysis that is often computationally prohibitive. This paper presents an efficient data-assisted optimization approach for fault identification without using the finite element model iteratively. We formulate a many-objective optimization problem to identify the fault parameters, where response surfaces of impedance measurements are constructed through the Gaussian process-based calibration. To balance between the solution diversity and convergence, an ε-dominance-enabled manyobjective simulated annealing algorithm is established. As multiple solutions are expected, a voting score calculation procedure is developed to further identify those solutions that yield better implications regarding a structural health condition. The effectiveness of the proposed approach is demonstrated by the systematic numerical and experimental case studies.

**INDEX TERMS** Structural fault identification, piezoelectric impedance/admittance, meta-modeling, Gaussian process, many-objective optimization, simulated annealing, voting score.

#### I. INTRODUCTION

The timely and accurate identification of faults in aerospace, mechanical, marine, and infrastructure systems has received significant recent attention. Different from traditional, offline non-destructive testing and evaluation (NDT&E) techniques, e.g., X-ray inspection, where the effectiveness is limited to the close vicinity of the sensors employed, online structural health monitoring is often facilitated through actuating and then sensing/measuring dynamic responses such as waves/vibrations that can propagate quite far [13]. This yields much larger coverage area and higher inspection efficiency. The advent of many new transducer materials/devices and the advancement in microelectronics have resulted in rapid

The associate editor coordinating the review of this manuscript and approving it for publication was Dong Wang.

progress in this area. On the other hand, bottlenecks and unique challenges exist. Structures are continuous media, and parameters characterizing structural faults, i.e., location and severity, are continuous variables as well. Hence, structural faults have infinitely many possible patterns/profiles with typically small characteristic lengths, which are further compounded by various uncertainties. Intuitively, the dynamic response data collected by the monitoring system must be in high-frequency range (i.e., with small wavelengths) so features of small-sized faults can be captured. The key issues thus are: 1) how to effectively generate high-frequency sensing data; and 2) how to efficiently and accurately identify fault location and severity from the data [35].

Owing to their two-way electro-mechanical coupling, piezoelectric transducers are commonly used in structural health monitoring [15], [33]. One class of methods is

ultrasonic propagating wave-based, where these transducers are used as actuators and sensors. The change of transient wave (e.g., Lamb wave) patterns, as waves propagate through fault site, can be used to infer fault occurrence. While these methods lead to high detection sensitivity due to the high-frequency nature, it is difficult to use transient responses to identify fault, especially to quantify the severity. The piezoelectric transducers have also been employed in the electrical impedance- or admittancebased methods where a piezoelectric transducer is integrated (bonded/embedded) with the structure being monitored [20]. In these methods, the piezoelectric transducer is driven by a sinusoidal voltage sweep over a certain frequency range, and the electrical response (i.e., the resulted current) is measured to extract the impedance/admittance information. Owing to the electro-mechanical coupling, the piezoelectric impedance/admittance is directly related to the mechanical impedance of the underlying structure. Thus, the change of piezoelectric impedance/admittance signature with respect to that under the healthy baseline state can be used as fault indicator. These methods have shown effectiveness for a variety of structural faults including crack, corrosion, debonding, joint degradation, etc [26], [38]. The impedance/admittance can be measured in high-frequency range. A significant advantage is that in these methods the piezoelectric transducer serves as actuator and sensor simultaneously and the circuitry design is extremely simple requiring essentially only a small resistor, which leads to implementation convenience.

A major hurdle remains. In theory, identifying directly the fault location and severity from stationary responses such as impedances/admittances is possible, if a credible first-principle model such as finite element model of the healthy baseline is available. A linearized sensitivity matrix can be derived that links the structural property changes to the changes of harmonic response magnitudes measured. Such an inverse problem is usually severely under-determined. In order to characterize high-frequency impedance/admittance responses accurately, the finite element model must have high dimensionality. To pinpoint fault condition, we often divide the structure into several segments where the structural property in each segment is an unknown to be solved (because each segment is susceptible of fault occurrence). Therefore, the model has high dimensionality with a large number of unknowns. Meanwhile, structural faults manifest themselves in structural resonances and anti-resonances. As such, the effective measurements of impedance/admittance changes are limited [30]. One potential way to avoid the direct inversion is to convert the identification problem into an optimization problem, where possible property changes in all segments are treated as design parameters. These parameters are updated by minimizing the discrepancy between sensor measurements and model predictions through various optimization techniques in which only forward analyses are performed [2], [6], [7], [27]. The necessary computational cost, however, could be very high. The forward optimization generally requires large number of iterations to converge, while a single run of high-dimensional finite element analysis can be very costly already.

Dynamic response calibration, as a faster alternative to exhaustive finite element analysis, has shown promising aspects in alleviating computational burden by emulating the full-scale finite element model responses. Traditional response surface methods applied for model updating use explicit functions to represent the relation between inputs and outputs. Least square-based techniques are then devised to refine parameters in the polynomial representation [12], [24], [28], [41], [42], (Chakrarborty and Sen, 2014). More recently, Gaussian process, also referred to as Kriging [19], [29], has gained popularity due to its capability to simulate complicated process subjected to uncertainties. A Gaussian process model is not restricted to certain polynomial form thus allows highly flexible modeling in input-output relation based on statistical expectations and variances over functions. Gao et al. [14] used a Kriging surrogate model to calibrate frequency responses for crack tip location identification in cantilever plates. Yang et al. [37] proposed a similar calibration approach in frequency domain to detect the location and severity of fault in small structures. Wan and Ren [32] suggested a residual-based Gaussian process model to characterize the relation between residual and updated parameters in frequency domain for finite element model updating. Jin and Jung [16] formulated a sequential surrogate modeling scheme that constructs multiple response surfaces for finite element model updating. Balafas et al. [3] presented a Gaussian process model in wavelet domain that can infer damage through hypothesis testing. It is worth noting that all these dynamic response calibration methods are applied to natural frequency measurements. Since in practice only lower-order natural frequencies can be realistically measured, the case setups in these studies are relatively simple with low dimensionality and the design parameters are discrete with low dimensionality as well. In comparison, in impedance/admittance sensing, considerably larger amount of measurements at many frequency points, can be acquired, and a high-dimensional structure is to be identified.

From the underlying physics standpoint, impedance/ admittance sensing offers a new opportunity to identify fault parameters more accurately for more complex structures. While the response calibration technique appears to be promising in possibly avoiding iterative finite element analyses in an optimization framework, new issue arises. Although fault effects are reflected in impedance/admittance change at each frequency point theoretically, the actual impedance/admittance measurements respond to a fault condition differently at different frequencies. Therefore, in order to correctly identify fault conditions, one would need to examine the impedance/admittance changes at many frequency points. In other words, in order to take full advantage of the high-frequency impedance/admittance sensing, we need to formulate and then solve efficiently an optimization problem to match response predictions with



measurements at many frequency points. It should be noted that *many-objective* global optimization usually features more than three objectives, while multi-objective optimization refers to that with no more than three objectives. Although it would appear to be easier to resort to weighted summation to solve a single objective optimization [14], [32], [37], weighting selection among objectives is ad-hoc, and the result could easily converge to a meaningless outcome due to multiple local optima, measurement noise and uncertainties.

In this research, we develop a new methodology of fault identification using piezoelectric impedance/admittance sensing. To thoroughly elucidate the health status, a manyobjective optimization is formulated to match parametric prediction with measurements at all frequency points of interest. Gaussian process regression is incorporated to construct the response surfaces, which not only significantly reduces computational cost but also yields continuous searching of fault parameters. Our goal in optimization is to find many solutions (owing to the under-determined nature of the problem) that are all optimal. In order to balance between solution convergence and diversity, we establish an  $\varepsilon$ -dominance enabled many-objective simulated annealing algorithm. Subsequently, inspired by concepts in social statistics, i.e., voting power and majority voting [31], a voting framework is employed to evaluate quality of the solutions obtained. Our proposed many-objective evaluation approach is able to distinguish the solutions that could accurately indicate the health condition of the structure and ultimately provide guidance for detailed examination.

The novelty of this new framework is multifold. This is the first research effort to use response surfaces of Gaussian process as objective functions for optimization, whereas the solution (i.e., fault identification result) is obtained by combining multi-objective Simulated Annealing with  $\varepsilon$ -dominance. The voting score calculation based on the outcome of manyobjective optimization is newly developed and successfully applied in this manuscript. The rest of this paper is organized as follows. In Section II, we establish the manyobjective optimization formulation assisted by Gaussian process regression for piezoelectric impedance active sensing, where the  $\varepsilon$ -dominance enabled many-objective approach and the voting score calculation are presented in detail. In Section III, the proposed method is evaluated through numerical case studies. Experimental validations are conducted in Section IV. Finally, concluding remarks are given in Section V.

# II. APPROACH FORMULATION

# A. PIEZOELECTRIC IMPEDANCE/ADMITTANCE ACTIVE SENSING

In piezoelectric impedance/admittance-based fault identification, a piezoelectric transducer circuit is attached to or embedded in a host structure. Harmonic excitation voltage with sweeping frequency, referred to as the excitation frequency or driving frequency, is supplied to actuate structural oscillation. The local structural oscillation in turn induces electrical response of the transducer due to electromechanical coupling. We can write the equations of motion of the coupled system in the finite element form as [34],

$$\mathbf{M\ddot{q}} + \mathbf{C\dot{q}} + \mathbf{Kq} + \mathbf{K_{12}}Q = \mathbf{0}$$
 (1a)

$$K_c Q + \mathbf{K}_{12}^{\mathbf{T}} \mathbf{q} = V_{\text{in}} \tag{1b}$$

where M, K and C are the mass matrix, stiffness matrix and damping matrix, respectively,  $\mathbf{q}$  is the structural displacement vector,  $\mathbf{K}_{12}$  is the electro-mechanical coupling vector due to piezoelectric effect,  $K_c$  is the reciprocal of the capacitance of the piezoelectric transducer, Q is the electrical charge on the surface of the piezoelectric transducer, and  $V_{\rm in}$  is the excitation voltage. Clearly in Equation (1), the impedance/admittance of the transducer is directly related to the impedance of the underlying structure and thus can be used as damage indicator. Under harmonic excitation, Equation (1) can be expressed in frequency domain. The admittance (reciprocal of impedance) of the piezoelectric transducer is then given as,

$$Y(\omega) = \frac{\dot{Q}}{V_{\text{in}}} = \frac{\omega i}{K_c - \mathbf{K}_{12}^T (\mathbf{K} - \mathbf{M}\omega^2 + \mathbf{C}\omega i)^{-1} \mathbf{K}_{12}}$$
(2)

where  $\omega$  is the excitation frequency and i is the imaginary unit. In discretized model-based fault identification, structural fault or damage is frequently assumed as local property change, e.g., local stiffness loss. We divide the host structure into n segments and use  $\mathbf{k}_{hj}$  to represent the stiffness matrix of the j-th segment under healthy condition. The stiffness matrix of the structure when fault occurs can be written as,

$$\mathbf{K}_d = \sum_{j=1}^n \mathbf{k}_{hj} (1 - \alpha_j) \tag{3}$$

where the summation refers to the usual direct sum involved in finite element matrix assemblage,  $\alpha_j \in [0, 1]$  is the fault index indicating the ratio of stiffness loss in the j-th segment. For example, if the j-th segment suffers from damage with a 10% stiffness loss, then  $\alpha_j = 0.1$ , otherwise  $\alpha_j = 0$ .  $\alpha = [\alpha_1, \cdots, \alpha_n]^T$  is the fault index vector. As the piezoelectric transducer and the underlying structure form a coupled system, structural fault will be reflected through the admittance of the piezoelectric transducer,

$$Y_d(\omega, \boldsymbol{\alpha}) = \frac{\dot{Q}_d}{V_{\text{in}}} = \frac{\omega i}{K_c - \mathbf{K}_{12}^T (\mathbf{K}_d - \mathbf{M}\omega^2 + \mathbf{C}\omega i)^{-1} \mathbf{K}_{12}}$$
(4)

The measured admittance of the structure with fault can then be compared with the baseline admittance to elucidate the health condition. The change of admittance before and after fault occurrence can be written as a function of excitation frequency  $\omega$  and damage index vector  $\alpha$ ,

$$\Delta Y(\omega, \boldsymbol{\alpha}) = Y_d(\omega, \boldsymbol{\alpha}) - Y(\omega, \boldsymbol{\alpha} = \boldsymbol{0})$$

$$= \frac{\omega i(\mathbf{k}_h \mathbf{1} - \mathbf{M}\omega^2 + \mathbf{C}\omega i)(\mathbf{k}_h \boldsymbol{\alpha} - \mathbf{M}\omega^2 + \mathbf{C}\omega i)}{-\mathbf{K}_{12}^T \mathbf{k}_h}$$
(5)

In Equation (5),  $\mathbf{k}_h = [\mathbf{k}_{h1}, \cdots, \mathbf{k}_{hm}]$ , which represents the stiffness sub-matrices of n segments when the structure is healthy. In impedance/admittance-based fault identification, as harmonic voltage excitation is supplied for active sensing, Equation (5) is used iteratively giving different read of  $\Delta Y(\omega, \alpha)$  when the excitation frequency is swept within certain ranges that cover a number of structural resonances around which physical measurements are taken. In order to characterize high-frequency responses, the finite element model must have high dimensionality. It is worth noting that the active-sensing fault identification framework is effective in giving implications of severity and location of the fault by means of stiffness change but limited in distinguishing the exact type.

#### B. DATA-ASSISTED IMPEDANCE RESPONSE CALIBRATION

As indicated in Introduction, direct inverse analysis based on Equation (5) generally yields a severely under-determined problem. One possible solution is to perform repeated forward finite element analyses in the parametric space within an optimization framework to identify fault parameters. In order to render such a procedure computationally tractable, in this sub-section we present a data-assisted meta-modeling approach through Gaussian process (GP) regression [17], [19], [29], (Stein, 2012). Essentially, we aim at rapidly constructing the response surfaces in the parametric space through emulations using experimental and/or numerical simulation data.

Gaussian process (GP) regression is an interpolation approach by which various spatial and temporal problems can be modeled [18], [35], [36]. For impedance-based active sensing, the observed output can be symbolized and denoted as  $\Delta Y(\mathbf{x}) = f(\mathbf{x}) + \varphi$ , where  $f(\mathbf{x})$  is the output of the numerical model,  $\mathbf{x}$  is the input vector, and  $\varphi$  is the model discrepancy. The additive error  $\varphi$  is assumed to follow an independent, identically distributed Gaussian distribution  $\varphi \sim N(0, \sigma_n^2)$ . A function  $\phi(\mathbf{x})$  can be introduced to map the input  $\mathbf{x}$  to  $f(\mathbf{x})$  as,

$$f(\mathbf{x}) = \phi(\mathbf{x})^T \mathbf{w} \tag{6}$$

where  $\mathbf{w}$  is a vector of unknown parameters. The probability density of the set of training samples  $(\Delta \mathbf{Y}, \mathbf{X})$  given  $\mathbf{w}$  can then be obtained,

$$p(\Delta \mathbf{Y} | \mathbf{X}, \mathbf{w}) = \prod_{i=1}^{n} p(\Delta Y_i | \mathbf{x}_i, \mathbf{w})$$

$$= \prod_{i=1}^{n} \frac{1}{\sqrt{2\pi}\sigma_n} \exp(-\frac{(\Delta Y_i - \phi(\mathbf{x}_i)^T \mathbf{w})^2}{2\sigma_n^2})$$

$$\sim N(\phi(\mathbf{x})^T \mathbf{w}, \sigma_n^2 \mathbf{I})$$
(7)

The training samples can be acquired either experimentally or from a credible finite element model. Now we assume a multivariate Gaussian prior over the parameters  $\mathbf{w} \sim N(\mathbf{0}, \Sigma_p)$  with zero mean and certain covariance. We can obtain the posterior probability density of  $\mathbf{w}$  through Bayes'

theorem.

$$p(\mathbf{w}|\mathbf{X}, \Delta \mathbf{Y}) = \frac{p(\Delta \mathbf{Y}|\mathbf{X}, \mathbf{w})p(\mathbf{w})}{p(\Delta \mathbf{Y}|\mathbf{X})} \sim (\sigma_n^{-2} A^{-1} \phi(\mathbf{x}) \Delta \mathbf{Y}, A^{-1})$$
(8)

where  $A = \sigma_n^{-2} \phi(\mathbf{x}) \phi(\mathbf{x})^T + \Sigma_p^{-1}$ . Finally, by averaging over all possible parameter values, the predictive distribution of  $f_*$  given a test input vector  $\mathbf{x}_*$  also follows Gaussian distribution,

$$p(f_* | \mathbf{x}_*, \mathbf{X}, \Delta \mathbf{Y})$$

$$= \int p(f_* | \mathbf{x}_*, \mathbf{w}) p(\mathbf{w} | \mathbf{X}, \Delta \mathbf{Y}) d\mathbf{w}$$

$$\sim N(\sigma_*^{-2} \phi(\mathbf{x}_*)^T A^{-1} \phi(\mathbf{x}) \Delta \mathbf{Y}, \phi(\mathbf{x}_*)^T A^{-1} \phi(\mathbf{x}_*))$$
(9)

Therefore, any finite number of outputs  $f_*$  given multiple test inputs  $\mathbf{x}_*$  have a joint Gaussian distribution. To define such distribution over the stochastic process  $f(\mathbf{x})$ , a Gaussian process regression model is developed,

$$f(\mathbf{x}) \sim GP(m(\mathbf{x}), k(\mathbf{x}, \mathbf{x}'))$$
 (10)

Equation (10) is fully specified by its mean function  $m(\mathbf{x})$  and covariance function or kernel  $k(\mathbf{x}, \mathbf{x}')$  where  $\mathbf{x}$  and  $\mathbf{x}'$  are in either the training or the test sets. For prior  $\mathbf{w} \sim N(\mathbf{0}, \Sigma_p)$ , the mean and covariance functions that determine the smoothness and variability are written as,

$$m(\mathbf{x}) = \mathbf{E}[f] = \phi(\mathbf{x})^T E[\mathbf{w}] = \mathbf{0}$$
 (11)

$$k(\mathbf{x}, \mathbf{x}') = \mathbb{E}[(f - m)(f' - m')] = \phi(\mathbf{x})^T \Sigma_p \phi(\mathbf{x}')$$
 (12)

The joint distribution of observation  $\Delta Y$  and unknown output  $f_*$  given training input set X and test input set  $X_*$  is then,

$$\begin{bmatrix} \Delta \mathbf{Y} \\ \mathbf{f}_* \end{bmatrix} \sim N \left( \mathbf{0}, \begin{bmatrix} K(\mathbf{X}, \mathbf{X}) + \sigma_n^2 \mathbf{I} & K(\mathbf{X}, \mathbf{X}_*) \\ K(\mathbf{X}_*, \mathbf{X}) & K(\mathbf{X}_*, \mathbf{X}_*) \end{bmatrix} \right)$$
(13)

 $K(\mathbf{X}, \mathbf{X}_*)$  denotes the  $n \times n_*$  matrix of kernels evaluated at all pairs of training and test points through  $k(\mathbf{x}, \mathbf{x}_*)$  for n training samples and  $n_*$  test inputs. Finally, the key predictive distribution of Gaussian process regression, i.e., the conditional distribution of  $\mathbf{f}_*$ , is expressed as

$$p(\mathbf{f}_* | \mathbf{X}_*, \mathbf{X}, \Delta \mathbf{Y}) \sim N(K(\mathbf{X}_*, \mathbf{X})[K(\mathbf{X}, \mathbf{X}) + \sigma_n^2 \mathbf{I}]^{-1} \Delta \mathbf{Y},$$
  
$$K(\mathbf{X}_*, \mathbf{X}_*) - K(\mathbf{X}_*, \mathbf{X})[K(\mathbf{X}, \mathbf{X}) + \sigma_n^2 \mathbf{I}]^{-1} K(\mathbf{X}, \mathbf{X}_*)) \quad (14)$$

which is the function-space view of Equation (9). In this research, the input vector is given as  $\mathbf{x} = [\omega, \alpha] \Leftrightarrow [\omega, \alpha_L, \alpha_S]$ , where  $\omega$  is the excitation frequency, and  $\alpha$  is the fault index vector. The vector  $\alpha$  can be further expressed as  $[\alpha_L, \alpha_S]$  for single fault cases, where  $\alpha_L$  is the location and  $\alpha_S$  is the severity. For example, if a structure is divided into 6 segments and the  $3^{\rm rd}$  segment is subjected to 5% damage (5% stiffness loss), then  $\alpha = [0, 0, 0.05, 0, 0, 0]$  or  $\alpha \Leftrightarrow [\alpha_L, \alpha_S] = [3, 0.05]$ . For each given  $\omega_j(j = 1, 2, \ldots, l)$  where l is the number of frequency points swept during inspection, if m observations or training data in Gaussian process regression can be obtained as  $\mathbf{D}_j = \{(\Delta Y_{ji}, \alpha_{Li}, \alpha_{Si}) | i = 1, 2, \ldots, m\}$ , we can then have l calibrations trained by  $\{\mathbf{D}_1, \mathbf{D}_2, \ldots, \mathbf{D}_l\}$  with a Gaussian process regression model  $f(\alpha) \sim GP(\mathbf{0}, k(\alpha, \alpha'))$ . One of the most



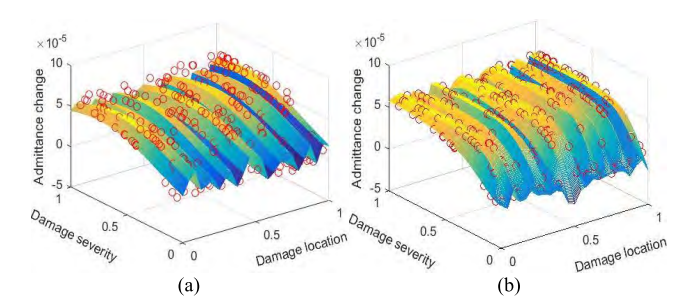


FIGURE 1. Admittance change calibrations (a) single squared exponential kernel (b) product of squared exponential kernels ( $\bigcirc$ : training sample).

widely-adopted kernel functions is the squared exponential function [29],

$$k(\boldsymbol{\alpha}, \boldsymbol{\alpha}') = \theta_1 \exp\left(\frac{\left|\boldsymbol{\alpha} - \boldsymbol{\alpha}'\right|^2}{\theta_2}\right)$$
 (15)

which is efficient toward cases where the training data is of the same type but in different dimensions. For inputs that have more than one type of feature, such as  $[\alpha_L, \alpha_S]$  characterizing location and severity that are different in nature, a well-accepted way to build a kernel is to multiply kernels together [11]. In this research, we adopt the product of two squared exponential functions as kernel,

$$k(\boldsymbol{\alpha}, \boldsymbol{\alpha}') = \theta_1 \exp\left(\frac{\left|\boldsymbol{\alpha} - \boldsymbol{\alpha}'\right|^2}{\theta_2}\right) \cdot \theta_3 \exp\left(\frac{\left|\boldsymbol{\alpha} - \boldsymbol{\alpha}'\right|^2}{\theta_4}\right)$$
(16)

The hyper-parameters  $\theta$  used in kernel are trained by maximizing the marginal likelihood  $p(\Delta \mathbf{Y} | \mathbf{X})$ , or the log marginal likelihood w.r.t.  $\theta$  and  $\sigma_n$ ,

$$\log p(\Delta \mathbf{Y} | \boldsymbol{\alpha}) = -\frac{1}{2} \Delta \mathbf{Y}^{T} (K(\boldsymbol{\alpha}, \boldsymbol{\alpha}) + \sigma_{n}^{2} \mathbf{I})^{-1} \Delta \mathbf{Y}$$
$$-\frac{1}{2} \log \left| K(\boldsymbol{\alpha}, \boldsymbol{\alpha}) + \sigma_{n}^{2} \mathbf{I} \right| - \frac{n}{2} \log 2\pi \quad (17)$$

The parameters are then evaluated using Markov chain Monte Carlo method [25] in this study.

Compared to single squared exponential kernel (Equation (15)), the product of squared exponential kernels (Equation (16)) can better represent the training samples in impedance-based fault identification. As shown in Figure 1, admittance changes are calibrated using single squared exponential function as kernel and product of squared exponential functions as kernel, respectively, given 270 training data. The calibration surface is the mean value of the predictive distribution acquired using Equation (14).

For l frequencies  $\omega_j(j = 1, 2, ..., l)$  swept by a piezoelectric transducer in active sensing, if l sets of training data  $\mathbf{D}_j$  are available either by experiment or from a finite element model, l calibration surfaces similar to Figure 1(b) can be developed,

$$\Delta Y_{1}^{(c)}(\alpha_{L}, \alpha_{S}) | \mathbf{D}_{1}$$

$$\vdots$$

$$\Delta Y_{l}^{(c)}(\alpha_{L}, \alpha_{S}) | \mathbf{D}_{l}$$
(18)

where  $\Delta Y_j^{(c)}$  represents the output of the reconstructed surface for any input  $(\alpha_L, \alpha_S)$  under excitation frequency  $\omega_j$ .

The proposed method therefore utilizes the regression models to reproduce responses by given different arguments of the response surfaces (health condition of the structure), where the analytical sensitivity matrix to correlate variables with the response is not involved. By minimizing the discrepancy between the predictions made by reconstructed surfaces and the actual measurements, the fault identification problem is essentially cast into an optimization problem. The impedance/admittance changes measured physically under the same l excitation frequencies  $\Delta Y_l^{(m)}$  are used to form l objective functions,

$$\min J_{1} = \left| \Delta Y_{1}^{(c)}(\alpha_{L}, \alpha_{S}) - \Delta Y_{1}^{(m)} \right|$$

$$\vdots$$

$$\min J_{l} = \left| \Delta Y_{l}^{(c)}(\alpha_{L}, \alpha_{S}) - \Delta Y_{l}^{(m)} \right|$$
(19)

where  $\alpha_S$  and  $\alpha_L$  are the design variables of the optimization problem. Consider the case where only one objective function  $J_1$  is employed. Minimizing merely  $J_1$  will possibly yield a large number of wrong solutions because it is an underdetermined problem with only one measurement subjected to error. Clearly, more information regarding the health condition should be taken into consideration by employing more objective functions. This showcases the underlying reason we formulate a many-objective optimization problem. We aim to find the "overlapping consensus" among the available, many objective functions. It is, however, computationally challenging to solve such an optimization problem.

#### C. VOTING-EMPOWERED MANY-OBJECTIVE EVALUATION

In this study, the procedure of many-objective evaluation is composed of many-objective optimization, post-processing and reasoning. Many-objective optimization (MaOO) problems are defined as those with four or more objectives [9] where the results cannot be directly visualized through graphical means. In comparison, multi-objective optimization problems have two or three objective functions. To illustrate the difficulties associated with solving many-objective optimization problems, we first introduce the Pareto optimality based multi-objective optimization, which has seen extensive research efforts [5], [8], [21], [39], [40]. For multiobjective optimization, the Pareto optimality is defined in a broader sense that no other solution is superior to the Pareto optimal solutions when all objectives are considered. Following this, a general Pareto-based MaOO problem where n objectives are minimized simultaneously is specified as

$$Minimize f(\mathbf{x}) = \{f_1(\mathbf{x}), \dots, f_n(\mathbf{x})\}$$
 (20)

where  $\mathbf{x}$  is the decision vector and  $\mathbf{f}$  is the objective vector. When two sets of decision vectors are compared, the concept of dominance is involved. Assuming  $\mathbf{a}$  and  $\mathbf{b}$  are two decision vectors, the concept of Pareto optimality can be defined

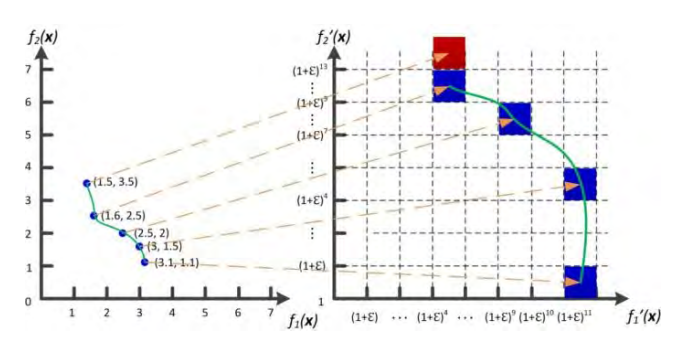


**FIGURE 2.** From Pareto optimal to  $\varepsilon$ -Pareto optimal.

as follows: a dominate b if:

$$\forall i = \{1, 2, \dots, n\} : f_i(\mathbf{a}) \le f_i(\mathbf{b})$$
 (21)

and

$$\exists j = \{1, 2, \dots, n\} : f_i(\mathbf{a}) < f_i(\mathbf{b})$$
 (22)

Any objective function vector, which is neither dominated by any objective function vector in the Pareto optimal set nor dominating any of them, is said to be non-dominated with respect to that Pareto optimal set. The solution that corresponds to the objective function vector is then a member of Pareto optimal set.

In comparison with multi-objective optimization, many-objective evaluation needs to tackle two major additional difficulties [9], [23]:

- 1) Almost all solutions generated are non-dominated to one another. As the number of objectives increases, even a mediocre solution could be Pareto optimal because it may have small advantages over other solutions in at least one objective, even though the differences are trivial. Consequently, most Pareto optimality-based multi-objective optimization algorithms become inefficient and out of focus when dealing with many objectives. The solution set yielded may be arbitrarily large.
- 2) It is hard to maintain good diversity among the solution set in high dimensional space. Generally, it is computationally expensive to evaluate diversity for many objectives. Moreover, the conflict between convergence and diversity is aggravated in high dimension. Therefore, attempts to maintain diversity may hinder the numerical procedure from converging to the optimal solutions.

The difficulties can be alleviated by using a special domination principle that will adaptively discretize the Pareto optimal set and find a well-distributed set of solutions. A good choice to tackle the above-mentioned difficulties is the  $\varepsilon$ -dominance principle [21], which alters and discretizes the objective space into boxes defined by the power of  $(1 + \varepsilon)$ ,

$$\left\lfloor \frac{\log f_i}{\log(1+\varepsilon)} \right\rfloor \tag{23}$$

Equation (23) projects each objective function vector uniquely to one box, which can neutralize trivial improvements in any objectives. One example is shown in Figure 2,

TABLE 1. e-dominance relations.

Relation	Symbol	Interpretation in $\mathcal{E}$ -objective space	
box( <b>a</b> ) dominates box( <b>b</b> )	$box(\mathbf{a}) \prec box(\mathbf{b})$	box(a) is not worse than box(b) in all objectives and better in at least one objective	
box( <b>b</b> ) dominates box( <b>a</b> )	$box(\mathbf{b}) \prec box(\mathbf{a})$	box(b) is not worse than box(a) in all objectives and better in at least one objective	
Non- $\mathcal{E}$ - dominant to each other	$box(\mathbf{b}) \cong box(\mathbf{a})$	box(a) is worse than box(b) in some objectives but better in some other objectives	
Same box	$box(\mathbf{a}) = box(\mathbf{b})$	$box(\mathbf{a})$ equals $box(\mathbf{b})$	

one Pareto optimal solution (1.5, 3.5) in the original objective space is eliminated in the  $\varepsilon$ -Pareto optimal set because it is merely better in one objective but a lot worse in the other objective compared to solution (1.6, 2.5). And by keeping one solution per box, a bounded size solution set with good diversity could be obtained. The difficulties can thus be addressed by the  $\varepsilon$ -dominance transformation. Accordingly, the dominance relation based on  $\varepsilon$ -dominance is given in Table 1 where the box operator refers to Equation (23) and  $\prec$  is used to denote dominance relation between decision vectors.

We incorporate the  $\varepsilon$ -dominance technique into a previously developed Multi-objective Simulated Annealing algorithm [5], hereafter referred to as  $\varepsilon$ -MOSA/R. The pseudo-code of  $\varepsilon$ -MOSA/R is provided below.

In this newly proposed  $\varepsilon$ -MOSA/R, we use  $\varepsilon$ -dominance relation as well as the regular dominance relation to compare the new solution, the current solution and Archive. Algorithm Update renews the Archive when a better solution in  $\varepsilon$ -dominance sense is found and meanwhile assures that only one solution is maintained per  $\varepsilon$ -box. As Algorithm Re-seed and Algorithm Simulated Annealing are embedded, Algorithm Action takes place when a deteriorated solution is sampled. Instead of abandoning the solution directly, probability relaxations are devised so that either the deteriorated solution is accepted with a certain probability to escape local optima (Simulated Annealing) or the search direction is swerved towards known search space with good solutions for better efficiency (Re-seed). The concept of the amount of domination is used in computing the acceptance probability in Re-seed and Simulated Annealing [1]. Given two solutions a and b, the amount of domination is defined as

$$\Delta dom_{\mathbf{a},\mathbf{b}} = \prod_{i=1, f_i(\mathbf{a}) \neq f_i(\mathbf{b})}^{l} \left( \left| f_i(\mathbf{a}) - f_i(\mathbf{b}) \right| / R_i \right) \quad (24)$$

where l is the number of objectives and  $R_i$  is the range of the i-th objective for normalization. In this research, for all case studies to converge, the total number of iterations of  $\varepsilon$ -MOSA/R is set as 100,000, Tmax is 100, Tmin is  $10^{-4}$ , and the cooling rate  $\alpha$  is set as 0.8.

Ideally, if the calibration surfaces are perfect without error, using more objectives (i.e., incorporating more measurements) naturally yields solution sets of better accuracy.



#### **Algorithm** $\varepsilon$ - MOSA/R

Set Tmax, Tmin, # of iterations per temperature iter, cooling rate  $\alpha$ , k = 0

Initialize the  $Archive(\varepsilon$ -Pareto front)

Current solution = randomly chosen from Archive

While (T > Tmin)

**For** 1 : *iter* 

Generate a *new solution* vector in the neighborhood of *current solution* vector

If new solution falls into the same  $\varepsilon$ -box as any solutions in the *Archive* 

If new solution dominates k (k >= 1) solutions in the *Archive* 

Update

Else

Action

End if

**Else if** *new solution*  $\varepsilon$ -dominates k (k >= 1) solutions in the *Archive* 

**Update** 

Else if new solution  $\varepsilon$ -dominated by k (k >= 1) solutions in the Archive

Action

Else if *new solution* and *Archive* are non- $\varepsilon$ -dominant to each other

**Update** 

End if

**End for** 

k = k + 1

 $T = (\alpha^k) * Tmax$ 

**End While** 

#### Algorithm Update

Remove all *k* dominated solutions from the *Archive* Add *new solution* to the *Archive* 

Set new solution as current solution

When enough response surfaces are used, the solution set should contain only one solution that matches perfectly the fault scenario. However, owing to modeling and calibration errors, utilizing more objective functions does not necessarily associate with better performance. As seen in Equation (19), l objective functions can be formulated under l excitation frequencies. While  $\varepsilon$ -MOSA/R introduced could cope with such a many-objective optimization problem, the solution size would increase nonlinearly with l [10]. Therefore, it could be even harder for a greater number of calibration surfaces to reach the "overlapping consensus" in determining the structural damage. Although using some subsets of available calibrated surfaces can uncover a small set of trustworthy solutions for further analysis, using other subsets may return many erroneous results. Given the difficulties, guiding the algorithm to only a few optimal solutions or making an objective decision becomes critical in many-objective optimization.

#### **Algorithm** Action

If new solution and Archive are non-dominant to each other Set new solution as current solution

Else

If new solution dominated by current solution

Re-seed

Else

**Simulated Annealing** 

End If

End if

#### Algorithm Re-Seed

*new solution* is dominated by k (k >= 1) solutions in the *Archive* 

Set selected solution as the *i*-th solution  $i = \arg\min_{i \in A} (\Delta dom_{i,new})$ 

If  $\frac{1}{1 + \exp(-\Delta dom_{selected,new}/\max(T,1))} > \text{rand}(0,1)*$ Set selected solution as current solution

Else

## **Simulated Annealing**

#### End if

\* rand(0,1) generates a random number between 0 to1

In this research, inspired by social statistics [31] and ensemble learning [4], we introduce a voting score calculation based on the concepts of majority voting and voting power to evaluate the quality of the solutions generated using different sets of response surfaces as objective functions. As not all those l objective functions are essential or equally important, to reduce variance,  $N(N \le l)$  functions are randomly selected from the set as objectives of the many-objective optimization problem denoted as J, which can be deemed as input of the many-objective algorithm,

$$\mathbf{A} = \varepsilon - \text{MOSA/R}(\mathbf{J}) \tag{25}$$

where  $\mathbf{A} = \{\alpha_a, \alpha_b, \alpha_c, \ldots\}$  represents the set of Pareto optimal solutions obtained after one many-objective optimization.

As shown in Figure 3, the many-objective optimization proposed is carried out M times for N randomly selected response surfaces as objective functions different for each execution. Hence, we have,

$$\{\mathbf{A}_1, \mathbf{A}_2, \dots, \mathbf{A}_M\} = \varepsilon - \text{MOSA/R}(\{\mathbf{J}_1, \mathbf{J}_2, \dots, \mathbf{J}_M\}) \quad (26)$$

We use  $A_i$  to represent the solution set of the *i*-th execution of the optimization given objective function set  $J_i$ . The voting score for a specific solution is calculated as in the following manner.

Voting strategy 1.

$$vs(\boldsymbol{\alpha}_a) = \sum_{i=1}^{M} \left| \boldsymbol{\alpha}_a \bigcap \mathbf{A}_i \right| / \left| \mathbf{A}_i \right|$$
 (27)



#### **Algorithm** Simulated Annealing

$$\Delta dom_{avg} = \frac{\sum_{i=1}^{k} \Delta dom_{i,new}}{k}$$

If  $\frac{1}{1 + \exp(\Delta dom_{avg}/T)} > \text{rand}(0,1)$ Set new solution as current solution

End if

where  $|\alpha_a \cap A_i|$  equals to 1 if  $A_i$  contains  $\alpha_a$ . For example, if  $\alpha_a$  appears in optimal solution set  $A_1$ ,  $A_3$  and  $A_4$ , then  $vs(\alpha_a) = 1/|A_1| + 1/|A_3| + 1/|A_4|$ . As given in Equation (27), the solution set obtained after each execution of optimization is assigned a total voting score of one, meaning that the more solutions there are in one solution set, the less voting power per solution. The rationale behind such design is that we want to grant larger voting power to the solutions in smaller solution sets which are considered as less affected by error. Thereafter, the scores assigned are added altogether for each possible damage scenario and the ones with higher voting scores are more likely to give accurate implications about the true structural damage. As a result, we look for indications made by the calibrations rather than a decisive result, which is prone to error and hard to obtain owing to the under-determined nature of fault identification problems. Notably, by keeping one less digit after the decimal point in terms of damage severity  $\alpha_L$ , we can investigate the voting scores for possible severity ranges.

Voting strategy 2.

$$vs(\hat{\boldsymbol{\alpha}}_a) = vs(\alpha_{aL}, \text{round}(\alpha_{aS})) = \sum_{i=1}^{M} \left| \hat{\boldsymbol{\alpha}}_a \bigcap \mathbf{A}_i \right| / \left| \mathbf{A}_i \right| \quad (28)$$

The round operator (i.e., 'round' in Equation (28)) rounds the number to the nearest decimal with one less digit, and  $|\hat{\alpha}_a \cap \mathbf{A}_i|$  here gives the number of solutions belong to both  $\hat{\alpha}_a$  and  $\mathbf{A}_i$ .

Recall that voting score calculation is designed to endow certain solutions more voting power when the solution set is small. We go one step further by withdrawing the voting scores from the solution sets that exceed the average size of all solution sets instead of equally assigning each solution set a voting score of one.

Voting strategy 3.

$$vs_{partial}(\boldsymbol{\alpha}_a) = \sum_{i=1}^{M} \frac{I(|\mathbf{A}_i| \le |\bar{\boldsymbol{A}}|) \cdot (|\boldsymbol{\alpha}_a \cap \mathbf{A}_i|)}{|\mathbf{A}_i|}$$
 (29)

Voting strategy 4.

$$vs_{partial}(\hat{\boldsymbol{\alpha}}_a) = \sum_{i=1}^{M} \frac{I(|\mathbf{A}_i| \le |\bar{\boldsymbol{A}}|) \cdot (|\hat{\boldsymbol{\alpha}}_a \cap \mathbf{A}_i|)}{|\mathbf{A}_i|}$$
(30)

where  $I(|\mathbf{A}_j| \leq |\bar{\mathbf{A}}|)$  is a logic operation that the value of it is 1 if the argument is true and 0 otherwise. By applying either Equation (29) or (30) for post-processing, a higher level of

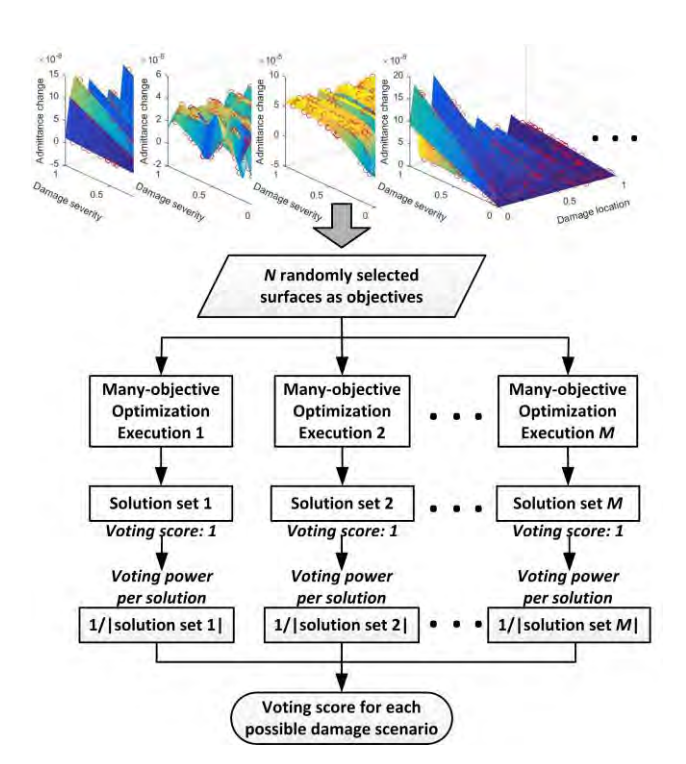


FIGURE 3. Voting score calculation for multi-objective evaluation.

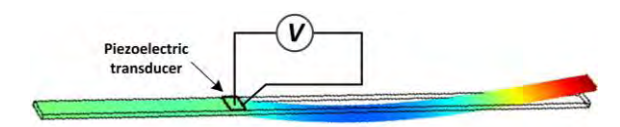


FIGURE 4. Illustration of structure for numerical case studies.

separation between insightful solutions and trivial solutions could be achieved.

In this study, we propose four decision making heuristics (Equations (27-30)) that essentially serve as four voting strategies to identify and isolate possible fault scenarios for further inspection. The randomness introduced when selecting response surfaces (Figure 3) as objective functions has desirable characteristics. It not only makes the evaluation scheme robust to outliers, but also gives useful internal estimates of noise such that we can withdraw voting scores from certain solution sets (Equations (29) and (30)). Moreover, it is compatible with parallel computing. Combined with Gaussian process regression and many-objective optimization, the proposed data-assisted many-objective evaluation framework is illustrated in detail through numerical and experimental case studies in Section III and Section IV, respectively.

# **III. NUMERICAL CASE STUDIES**

In this section, we carry out two numerical case studies to illustrate the proposed methodology and gain insights. The structure of interest is an aluminum cantilevered plate (Figure 4) with the following properties: length 0.561 m, width 0.01905 m, thickness 0.0014 m, density 2700 kg/m<sup>3</sup>, and Young's modulus 68.9 GPa. A piezoelectric transducer



is attached to the middle left of the plate, i.e., 0.18 m from the fixed end. The properties of the piezoelectric transducer are: length 0.015 m, width 0.01905m, thickness 0.0014 m, Young's moduli  $Y_{11} = 86$  GPa and  $Y_{33} = 73$  GPa, density 9500 kg/m<sup>3</sup>, piezoelectric constant  $-1.0288 \times 10^9$  V/m, and dielectric constant  $\beta_{33} = 1.3832 \times 10^8$  m/F. The finite element model of the plate contains 11,250 20-node hexahedron elements, the size of which is smaller than the shortest wavelength of the response involved in this study. The plate is further evenly divided into 25 segments lengthwise, each representing a possible damage location. In this research, we use finite element code developed by ourselves to carry out the investigations. This will facilitate a streamlined process to generate simulated responses of impedance/admittance as well as the segmentation procedure involved. The plate model used in the analysis is fully validated using ANSYS.

In structural health monitoring using impedance or admittance measurements, the response changes due to damage occurrence are most evident around the resonant peaks. In the following numerical case studies, we acquire admittance measurements at 40 excitation frequencies around the plate's 14<sup>th</sup>, 16<sup>th</sup>, 21<sup>st</sup> and 23<sup>rd</sup> natural frequencies. Specifically, the admittance values at 40 evenly distributed excitation frequencies in the ranges 1886.6 Hz to 1890.4 Hz, 2423.7 Hz to 2428.5 Hz, 3694.6 Hz to 3702.0 Hz and 4438.7 Hz to 4447.6 Hz are employed. Identical for each frequency, 270 randomly generated fault scenarios are emulated for the calibration of impedance response surface. The sampling range is specified as 1 to 25 for location and 0 to 0.1 for severity. In actual implementation, we can utilize experimentally acquired measurements directly. The data sampled from the model is contaminated by  $\pm 0.15\%$  standard Gaussian uncertainties to demonstrate the effectiveness of the proposed approach. We randomly selected fault scenarios that do not belong to the training set, i.e., damage occurring at the 13<sup>th</sup> segment with severity  $\alpha_{13} = 0.0600$  (6.00% stiffness loss in 13th segment), and at 22nd segment with severity  $\alpha_{22} = 0.0857$  (8.57% stiffness loss).

Figure 5 showcases all 40 impedance response surfaces using Gaussian process regression outlined in Section II-B, which serve as 40 objective functions. The two horizontal axes indicate damage location and severity (normalized), the vertical axis indicates the admittance change measured, and the red circle represents a training sample. The fidelity and effectiveness of response surfaces hinges upon the quality and quantity of samples. A general guideline is to sample as uniformly as possible, to capture the peaks and valleys. Certain response surface could be portrayed relative easily with less samples while the others requires more samples to be reliable, as shown in Figure 5. But we can use different combinations of surfaces as objective functions in each optimization for robust performance.

Based on the many-objective evaluation approach outlined in Section II-C (Figure 3), for each optimization practice,

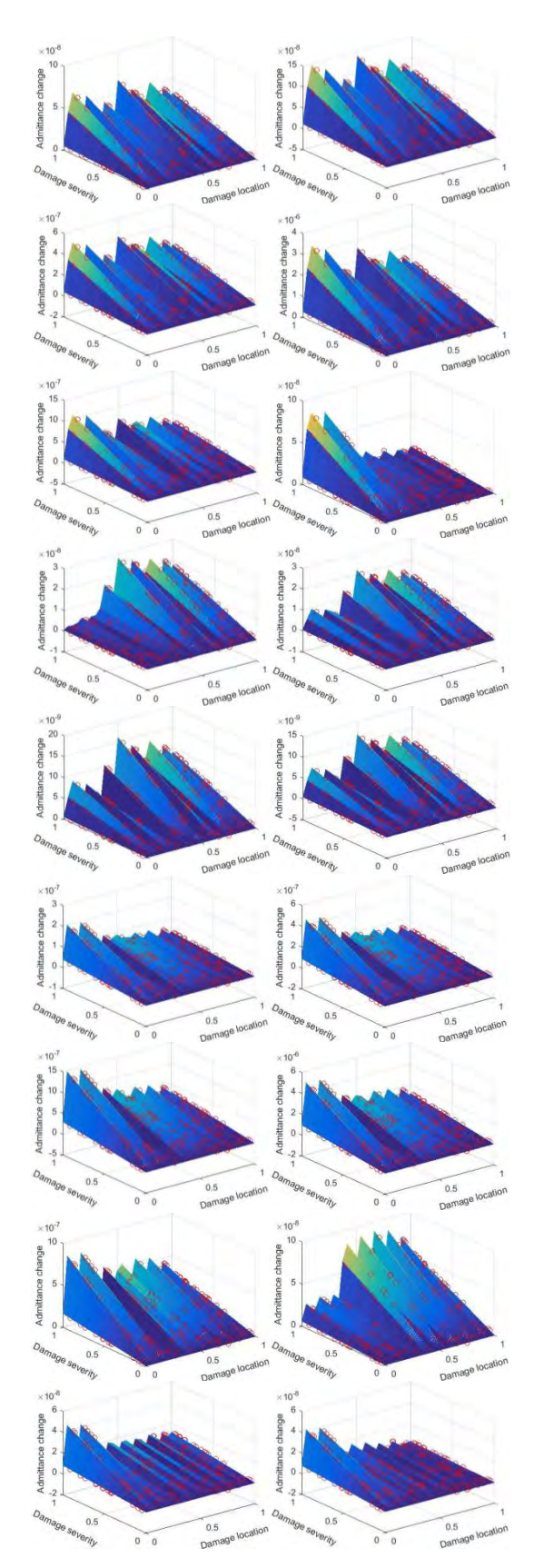


FIGURE 5. Calibrated response surfaces for 40 excitation frequencies ( denotes training point).

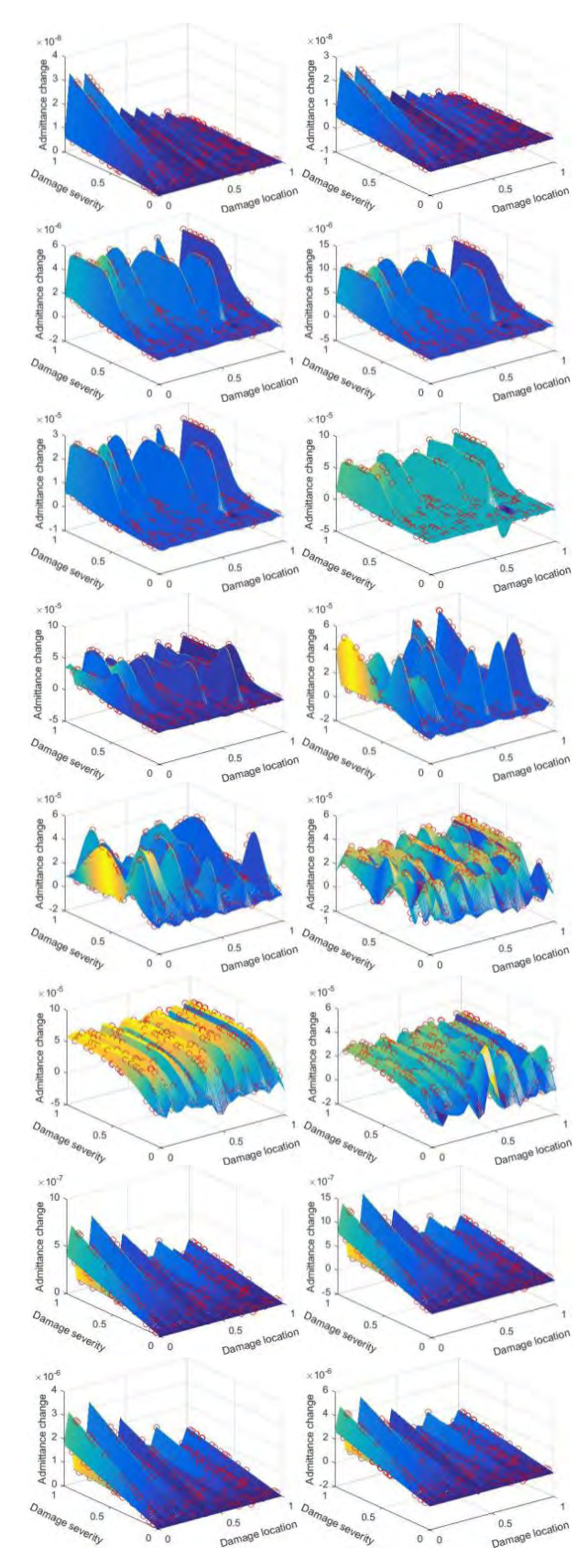


FIGURE 5. (Continued.) Calibrated response surfaces for 40 excitation frequencies ( $\bigcirc$  denotes training point).

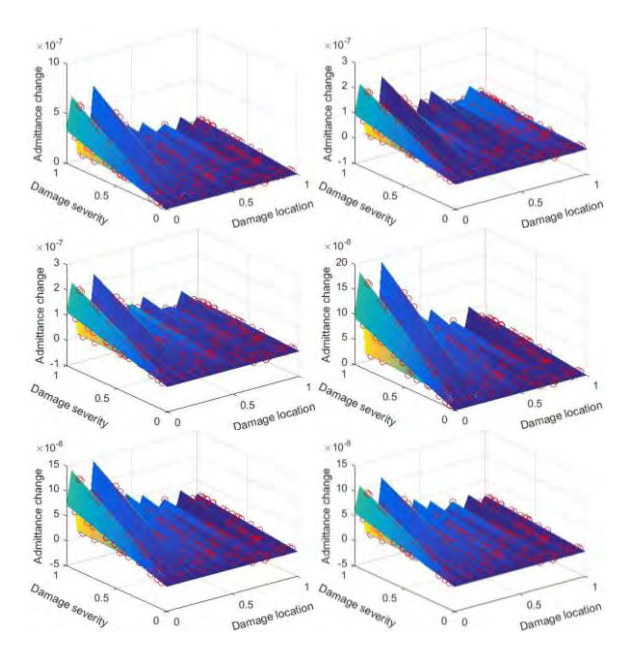


FIGURE 5. (Continued.) Calibrated response surfaces for 40 excitation frequencies ( $\bigcirc$  denotes training point).

10 (N=10) surfaces out of 40 are randomly selected as objective functions, to decouple each voting for robust performance. The many-objective optimization is executed  $30 \ (M=30)$  times. The parameter N is selected in accordance with the capacity of the many-objective optimization algorithm implemented, and the value of M should be set as large as possible for robustness. In this study, we use M=30 for illustration. In other words, a total of 30 voting scores are assigned to possible solutions obtained in 30 many-objective optimization practices.

## A. 6.00% STIFFNESS LOSS IN 13th SEGMENT

We first investigate the case where the 13<sup>th</sup> segment suffers from 6.00% stiffness loss. Here, the post-processing of MaOO introduced in Section II-C warrants detailed discussion. After performing the many-objective optimization, we obtain 369 solutions, or 369 possible fault scenarios. Voting score calculation (Equation (27)) is carried out successively accrediting score to each solution. As shown in Figure 6, the solution with the highest voting score agrees with the actual damage with only 0.0001 difference in stiffness loss ratio.

In the first voting strategy, four digits are kept for damage severity. By keeping one less digit after the decimal point following Equation (28), we are able to examine the voting scores for possible severity ranges, as plotted in Figure 7(a). Some are more distinct from the others compare to Figure 6. The range with the highest voting score indeed includes the induced fault (Table 2). We then withdraw the voting scores from those solution sets that exceed the average size following Equation (29). A total of 16 voting scores are to be distributed among possible solutions. As shown in Figure 7(b),



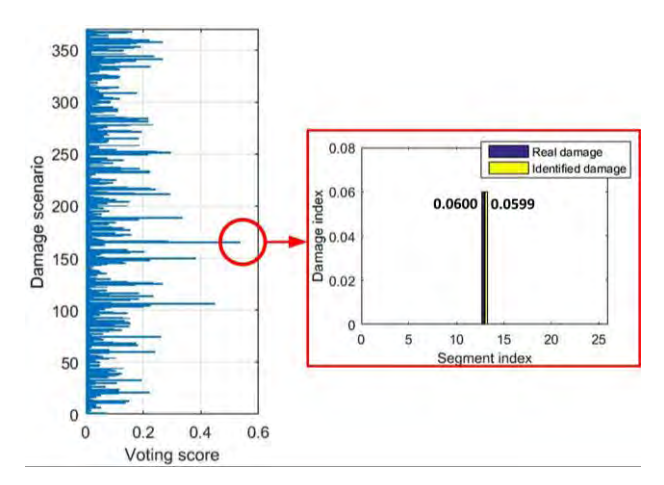


FIGURE 6. Voting strategy 1: 369 fault scenarios and the one with the highest score.

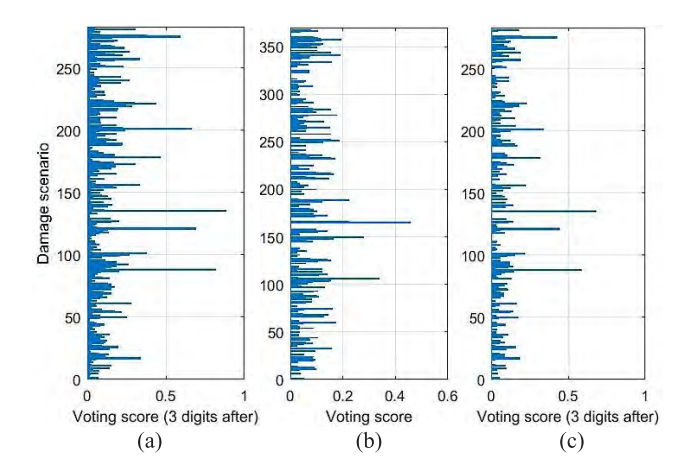


FIGURE 7. (a) Voting strategy 2: 282 fault ranges (b) Voting strategy 3: 369 fault scenarios (c) Voting strategy 4: 282 fault ranges.

some of the fault scenarios are now affiliated with zero scores. Meanwhile, the solutions with higher voting scores are significantly separated. Similarly, the voting scores for severity ranges can be inspected by grouping certain damage severities (Equation (30)) and, as illustrated in Figure 7(c), a greater separation is achieved.

The purpose of acquiring higher level of separation stems from the under-determined nature of such fault identification scheme due to insufficient measurements, uncertainties and errors. Thus, multiple solutions are expected. The proposed data-assisted many-objective evaluation seeks to isolate a small number of possible solutions for detailed inspections. In Figure 8, we observe that for each voting strategy, the percentage of voting score earned by the true fault is significantly higher than the average. The margin increases as we move from strategy one to four. The true fault is clearly favored and pinpointed among all possible fault scenarios using the proposed methodology.

Table 2 lists the fault scenarios with the three highest voting scores calculated. As shown, the ones with the highest scores all match or cover the true fault scenario. The percentage of

**TABLE 2.** Three fault scenarios with highest voting scores.

Voting strategy 1 (Equation (27))				
Fault scenario		Voting	Score %	
Segment	Severity	score	30 overall	
13	0.0599	0.5351	1.784%	
10	0.0522	0.4474	1.491%	
12	0.0532	0.3822	1.274%	
	Voting strategy 2 (Equation (28))			
Fau	lt scenario	Voting	Score %	
Segment	Severity range	score	30 overall	
13	0.0595~0.0605	0.8822	2.941%	
10	0.0515~0.0525	0.8137	2.712%	
12	0.0525~0.0535	0.6881	2.294%	
	Voting strategy 3 (E	quation (29))		
Fault scenario		Voting	Score %	
Segment	Severity	score	16 overall	
13	0.0599	0.4579	2.862%	
10	0.0522	0.3373	2.108%	
12	0.0532	0.2790	1.744%	
	Voting strategy 4 (Equation (30))			
Fault scenario		Voting	Score %	
Segment	Severity range	score	16 overall	
13	0.0595~0.0605	0.6794	4.246%	
10	0.0515~0.0525	0.5866	3.666%	
12	0.0525~0.0535	0.4434	2.771%	

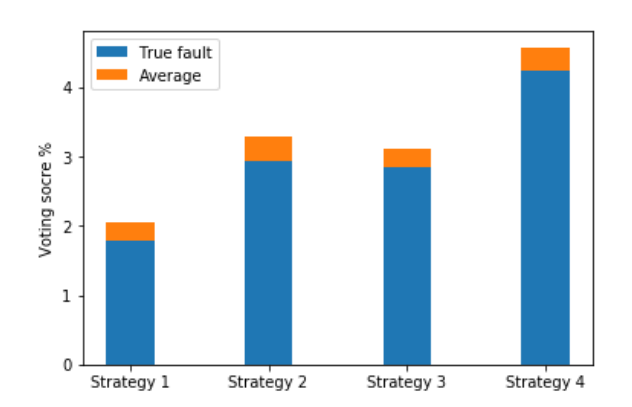


FIGURE 8. Voting score percentage of true fault compared to average.

voting score out of all voting scores being allotted is also reported. When prior knowledge is unavailable, solutions with relatively higher scores should be considered as candidates while the proposed voting score scheme filters out most of the unlikely scenarios. Therefore, even though one certain solution is hard, if not impossible, to obtain, only a few need to be examined with the help of many-objective evaluation, and the one with the highest voting score is more likely to match the true fault scenario.

# B. 8.57% STIFFNESS LOSS IN 22<sup>nd</sup> SEGMENT

To further demonstrate the approach, we look into another numerical case where the 22<sup>nd</sup> segment suffers 8.57% stiffness loss. Similarly, the four voting strategies are implemented, aiming to identify and distinguish the true fault in the host structure. Figure 9 depicts the voting score for the true fault in comparison with the average voting score. The proposed method accredits higher score to the true fault, and the

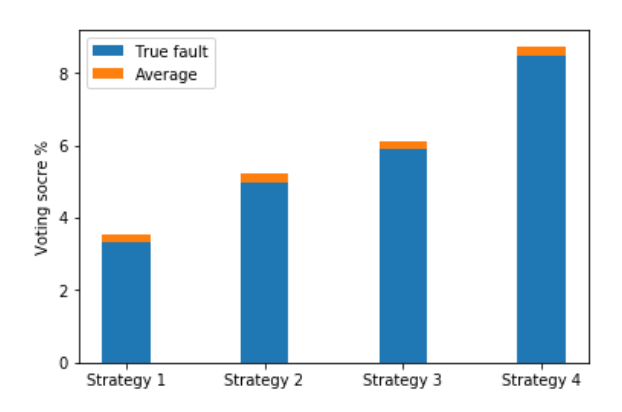


FIGURE 9. Voting score percentage of true fault compared to average.

**TABLE 3.** Three fault scenarios with highest voting scores.

	Voting strategy 1 (Eq	uation (27))		
Fa	ult scenario	Voting	Score %	
Segment	Severity	score	30 overall	
22	0.0856	1.0044	3.348%	
25	0.0813	0.7574	2.525%	
25	0.0923	0.6529	2.176%	
	Voting strategy 2 (Equation (28))			
Fa	ult scenario	Voting	Score %	
Segment	Severity range	score	30 overall	
22	0.0855~0.0865	1.4931	4.977%	
25	0.0915~0.0925	0.8741	2.914%	
25	0.0805~0.0815	0.7573	2.524%	
	Voting strategy 3 (Eq	uation (29))		
Fault scenario		Voting	Score %	
Segment	Severity	score	17 overall	
22	0.0856	1.0044	5.908%	
25	0.0813	0.7433	4.372%	
25	0.0923	0.5045	2.968%	
	Voting strategy 4 (Eq	uation (30))		
Fault scenario		Voting	Score %	
Segment	Severity range	score	17 overall	
22	0.0855~0.0865	1.444	8.494%	
25	0.0805~0.0815	0.7433	4.372%	
25	0.0915~0.0925	0.7257	4.269%	

indication towards the true fault becomes more pronounced when we progress through the voting strategies.

The results associated with the three highest voting scores are ranked in Table 3. Similar to the results reported in Section III-A, in this case study, the ones with the highest scores all agree with or cover the true fault scenario.

Here in this section, we also study the effectiveness of the proposed voting score calculation (Equation (27)) in discriminating possible damage scenarios. The idea of voting has also been used in ensemble learning such as random forest [4] and pattern recognition [22] to combine different sets of result where majority voting is implemented. Compared to the proposed voting score strategy, majority voting considers the one damage scenario that appears the most in all solution sets as the indication of true damage. Figure 10 compares the solution associated with the highest voting score, which concur with the true damage scenario, to the solution that appears the most among solution sets. As revealed in Table 4,

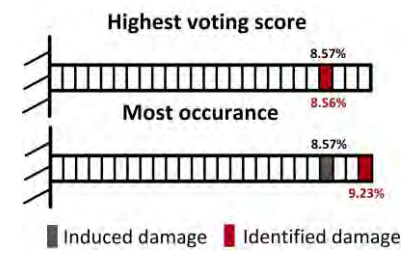


FIGURE 10. The fault scenario with the highest voting score vs. the damage scenario with the most occurrence.

**TABLE 4.** Top five fault scenarios: highest voting scores vs. most occurrences.

Proposed voting score strategy				
Damage scenario		Voting score		
Segment	Severity	30 overall		
22	0.0856	1.0044		
25	0.0813	0.7574		
25	0.0923	0.6529		
Major	Majority voting (most occurrence)			
Damage	scenario	Occurrence		
Segment	Severity	1289 overall		
25	0.0923	17		
15	0.0682	16		
13	0.0946	15		

the voting score calculation successfully re-adjusts weights among all solutions. The voting heuristics manage to rank them essentially based on their quality and thus have better performance identifying the true fault. Indeed, the solution with the highest voting score is not only among the solutions that appear the most in the results of many-objective optimizations, but also is less affected by error. It appears mostly in small solution sets which are considered more insightful with less conflict between objective functions and more confidence. After all, the objective functions should not be contradicted with each other ideally without error.

#### IV. EXPERIMENTAL VALIDATION

In this section, experimental case studies using physical measurements of piezoelectric admittance are carried out. The experimental setup, geometry measures and material parameters are consistent with those used in the numerical analysis in Section III. Figure 10 shows the experimental setup. Since certain faults, such as erosion and crack, are hard to emulate under experimental conditions, we add a small mass to the host structure, which can result in the same resonant frequency shift and admittance change as a local stiffness reduction would. To obtain the admittance of the piezoelectric circuit, a resistor of 100  $\Omega$  is serially-connected to the transducer to measure the voltage drop, which is further used to extract the current in the circuit. An Agilent 35670A signal analyzer is employed, where the source channel is used to generate sinusoidal voltage sent to piezoelectric transducer denoted as  $V_{\rm in}$ , and the output voltage across the resistor is recorded as  $V_{\text{out}}$ . Hence, the admittance can be obtained as  $Y = I/V_{\text{in}} = V_{\text{out}}/R_sV_{\text{in}}$ . In experimental case studies,



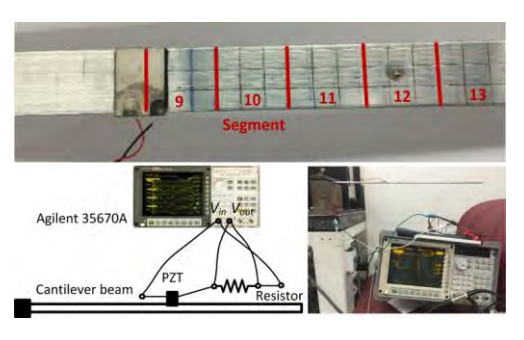


FIGURE 11. Experiment Setup.

we acquire measurement samples using 18 excitation frequencies around the plate's 14<sup>th</sup> and 21<sup>st</sup> natural frequencies. That is, 10 evenly distributed frequencies from the range 1886.6 Hz to 1890.4 Hz and 8 evenly distributed frequencies from the range 3696.2 Hz to 3702.0 Hz are acquired.

Identical for each frequency, 150 randomly generated damage scenarios are emulated for impedance response surface calibration using the corresponding numerical model. Figure 11 illustrates all 18 impedance response surfaces reconstructed by Gaussian process regression. In order to reduce the unwanted variations and uncertainties in this case illustration, instead of disassembling and cutting the plate to reduce the local stiffness, we add small masses to emulate the damage occurrence. Mathematically, adding a small mass can result in the same resonant frequency shift and admittance change as a local stiffness reduction would. In the first experiment, a 0.6 g mass is attached to the 14th segment of the plate, which causes admittance change equivalent to a 0.28% local stiffness loss. In the second experiment, the same mass is attached to the 12<sup>th</sup> segment, which is equivalent to a 0.16% local stiffness loss.

Based on the methodology proposed, the many-objective optimization is executed 10 times, and for each optimization execution, 10 surfaces out of 18 are randomly selected as objective functions. In other words, a total of 10 voting scores are assigned to solutions obtained.

# A. 0.28% STIFFNESS LOSS IN 14th SEGMENT

We first perform the experimental case study where the 14<sup>th</sup> segment is subjected to a 0.28% stiffness loss. Figure 12 plots the voting score percentage, which quantifies voting power, after many-objective optimization for the true fault scenario comparatively with the average of all possible fault scenarios. As uncertainties such as modeling error and measurement error are present inevitably in experimental case studies, the advantage of the true fault using voting strategy 1 is relatively modest. However, by examining the solutions based on the severity ranges they fall into (strategy 2), more confidence is gained. The visualizations of the solutions associated with the highest voting scores (Figure 13) imply accurate predictions is achieved based upon the proposed methodology. In practice, the solutions with relatively higher voting scores should be considered as candidates.

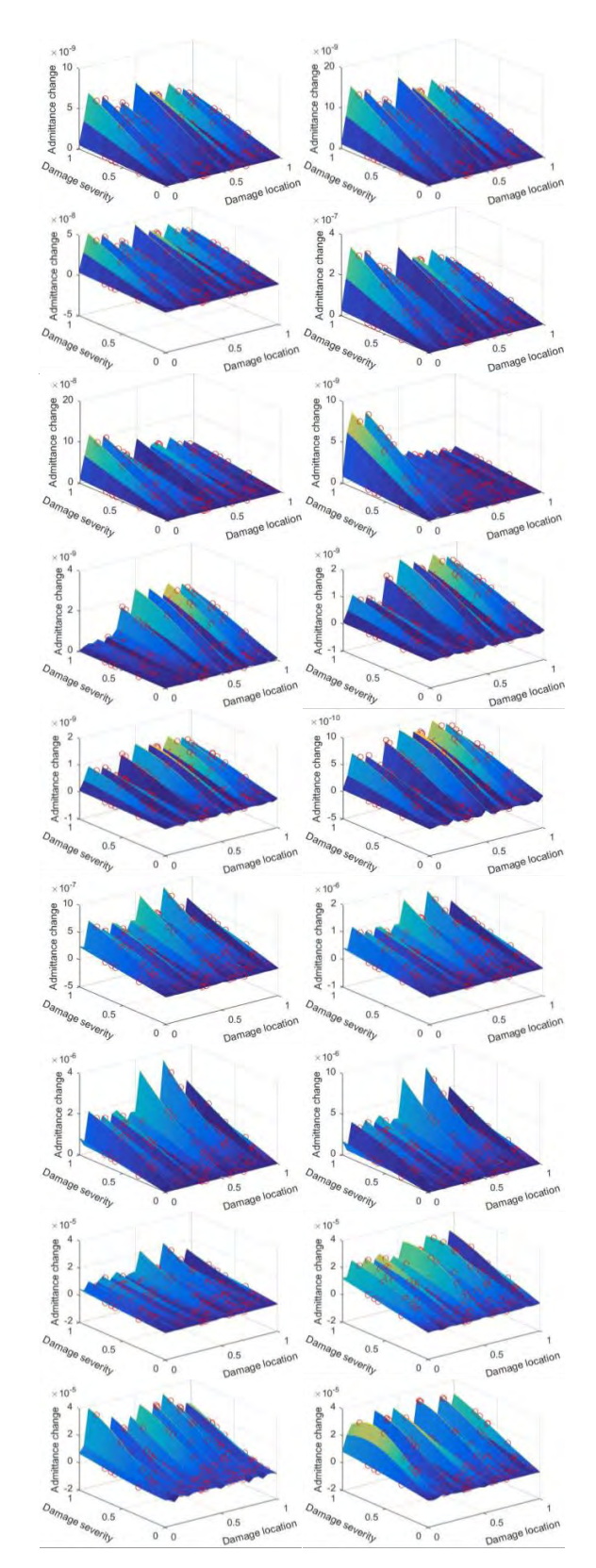


FIGURE 12. Calibrated response surfaces for 18 excitation frequencies from small to large (\( \) denotes training point).

Such candidate set provided could serves as the starting point for detailed inspections, which streamlines the typical procedure of inspection and maintenance in engineering practice.

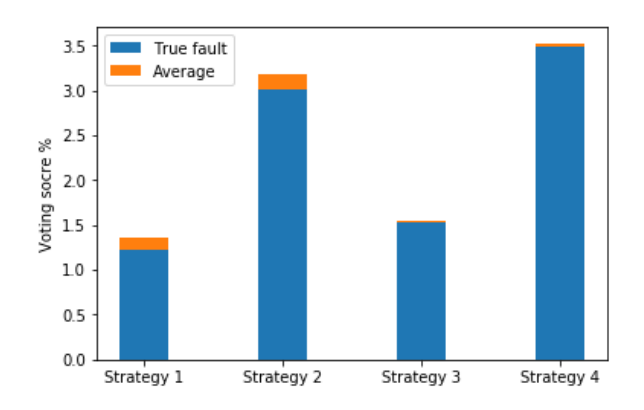


FIGURE 13. Voting score percentage of true fault compared to average.

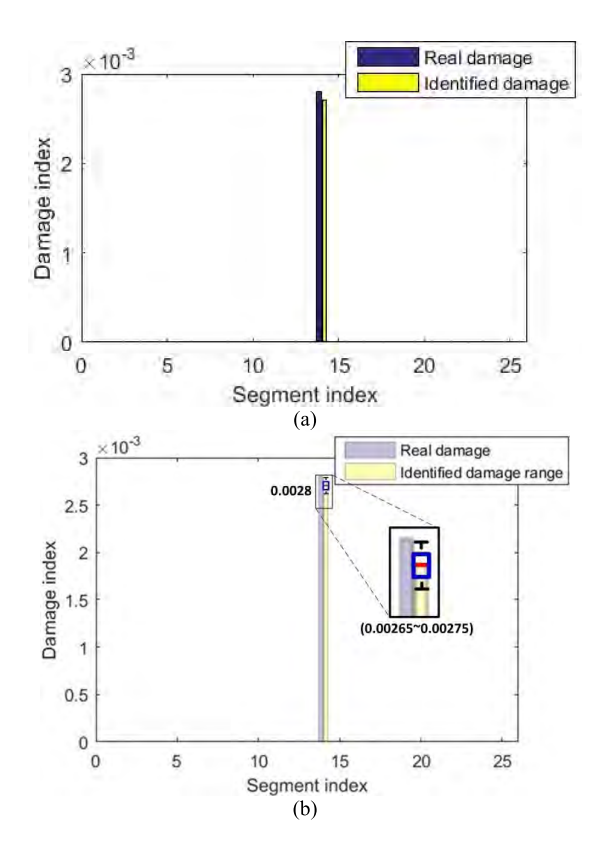


FIGURE 14. (a) Identified damage (the fault scenario with the highest voting score) (b) Identified damage range (the range with the highest voting score).

Next, by assigning zero voting scores to the solution sets that exceed the average size of all solution sets (strategy 3), we can probe some of the solutions provided by certain solution sets which are considered of better quality. As shown in Figure 12, a higher level of distinction is achieved among solutions using strategy 3 and 4. The detailed results are reported in Table 5 where the three damage scenarios with highest voting scores are demonstrated.

# B. 0.16% STIFFNESS LOSS IN 12th SEGMENT

The second experimental study concerns the case where the  $12^{th}$  segment is subjected to a 0.16% equivalent

TABLE 5. Three fault scenarios with highest voting scores.

	Voting strategy 1 (Ed	quation (27))	
Fault scenario		Voting score	Score %
Segment	Severity		10 overall
14	0.00271	0.1223	1.223%
5	0.00609	0.1153	1.153%
3	0.00294	0.1153	1.153%
	Voting strategy 2 (E	quation (28))	
F	ault scenario	Voting score	Score %
Segment	Severity range		10 overall
14	0.00265~0.00275	0.3016	3.016%
11	0.00715~0.00725	0.2078	2.078%
11	0.00705~0.00715	0.1882	1.882%
	Voting strategy 3 (E	quation (29))	
F	Fault scenario		Score %
Segment	Severity		6 overall
14	0.00271	0.0917	1.528%
6	0.00458	0.0789	1.315%
12	0.00645	0.0787	1.312%
	Voting strategy 4 (E	quation (30))	
F	ault scenario	Voting	Score %
Segment	Severity range	score	6 overall
14	0.00265~0.00275	0.2099	3.498%
11	0.00715~0.00725	0.1372	2.287%
11	0.00705~0.00715	0.1176	1.960%

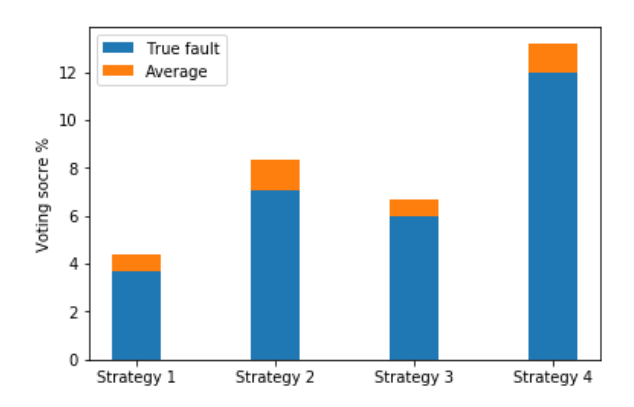


FIGURE 15. Voting score percentage of true fault compared to average.

stiffness loss. Figure 14 plots the average voting score percentages for all 139 possible fault scenarios and 71 severity ranges after many-objective evaluation stacked on top of the voting score percentage true fault received. It is noticed that, again, that the true fault scenario stands out in voting.

As shown in Figure 15, the solution with the highest voting score delivers close indication of the health condition of the structure. And if we consider the severity range with the highest voting score as the identified damage severity range, it also covers the true damage scenario. The actual voting power granted to a fault scenario is given by the ratio of the voting score percentage to the average percentage. For example, in Figure 14, the absolute voting score percentage of strategy 3 is lower than that of strategy 2, but it still has larger voting power due to the higher ratio to average percentage.

As can be seen in Table 6, for all four post-processing means, the ones with the highest voting scores all make accurate implications of the health condition of the structure.



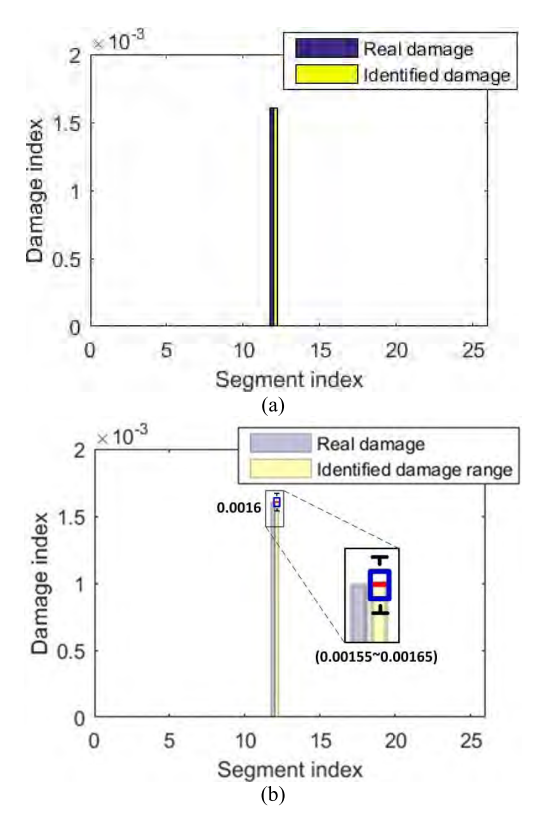


FIGURE 16. (a) Identified damage (the fault scenario with the highest voting score) (b) Identified damage range (the range with the highest voting score).

TABLE 6. Three fault scenarios with highest voting scores.

Voting strategy 1 (Equation (27))			
Damage scenario		Voting	Score %
Segment	Severity	score	10 overall
12	0.00161	0.3696	3.696%
12	0.00157	0.3355	3.355%
12	0.00154	0.2554	2.554%
	Voting strategy 2 (Eq	uation (28))	
Da	amage scenario	Voting	Score %
Segment	Severity range	score	10 overall
12	0.00155~0.00165	0.7050	7.050%
8	0.00135~0.00145	0.4467	4.467%
21	0.00145~0.00155	0.3232	3.232%
	Voting strategy 3 (Eq	uation (29))	
Damage scenario		Voting	Score %
Segment	Severity	score	4 overall
12	0.00160	0.2395	5.988%
12	0.00157	0.2395	5.988%
12	0.00154	0.1919	4.798%
Voting strategy 4 (Equation (30))			
Damage scenario		Voting	Score %
Segment	Severity range	score	4 overall
12	0.00155~0.00165	0.4791	11.978%
8	0.00135~0.00145	0.2316	5.790%
21	0.00145~0.00155	0.1962	4.910%

In practice, as we want to inspect only a small number of damage scenarios in maintenance, the overall approach proposed in this study can help to isolate a small set of the solutions that are more related to the health condition of the structure through its data-assisted analysis. Instead of seeking for one

deterministic solution that could be misguiding, the approach proposed in this research utilizes training data to analyze and identify probable fault scenarios that serve as guidance for further examination through heterogeneous sensing and inspection.

#### **V. CONCLUDING REMARKS**

This research presents a data-assisted approach for structural fault identification through Gaussian process-based impedance response calibration and many-objective evaluation. To address the fundamental challenges posed by the under-determined problem formulation and model-based sensitivity approximation, we cast the damage identification problem into a many-objective optimization by reconstructing impedance response surfaces as objective functions utilizing training data. The optimization problem is then tackled by an  $\varepsilon$ -dominance enabled many-objective simulated annealing algorithm. As many solutions are expected in manyoptimization practices, a voting score calculation procedure is developed and applied after to quantify and identify the solutions that could make better implication about the health condition of the structure. The numerical case studies and experimental case studies demonstrate that the proposed approach is capable of obtaining a small set of solutions based on their voting scores that could provide accurate implication about the health condition of the interested structure. The proposed scheme is inherently malleable and can be applied to either model-based or model-free fault identification systems wherever data is available. The combination of Gaussian process-based calibration, many-objective optimization, and voting score calculation can be extended to a variety of inverse analysis problems.

#### REFERENCES

- S. Bandyopadhyay, S. Saha, U. Maulik, and K. Deb, "A simulated annealing-based multiobjective optimization algorithm: AMOSA," *IEEE Trans. Evol. Comput.*, vol. 12, no. 3, pp. 269–283, Jun. 2008.
- [2] O. Begambre and J. E. Laier, "A hybrid particle swarm optimization—simplex algorithm (PSOS) for structural damage identification," *Adv. Eng. Softw.*, vol. 40, no. 9, pp. 883–891, 2009.
- [3] K. Balafas, A. S. Kiremidjian, and R. Rajagopal, "The wavelet transform as a Gaussian process for damage detection," *Struct. Control Health Monitoring*, vol. 25, no. 2, p. e2087, 2018.
- [4] L. Breiman, "Random forests," Mach. Learn., vol. 1, no. 45, pp. 5–32, 2001.
- [5] P. Cao, Z. Fan, R. Gao, and J. Tang, "A manufacturing oriented single point search hyper-heuristic scheme for multi-objective optimization," in *Proc.* ASME Int. Design Eng. Tech. Conf. Comput. Inf. Eng. Conf. Amer. Soc. Mech. Eng., 2017, Art. no. V02BT03A031.
- [6] P. Cao, Q. Shuai, and J. Tang, "A multi-objective DIRECT algorithm towards structural damage identification with limited dynamic response information," ASME J. Nondestruct. Eval., Diagnostics Prognostics Eng. Syst., vol. 1, no. 2, 2018, Art. no. 021004.
- [7] P. Cao, Q. Shuai, and J. Tang, "Structural damage identification using piezoelectric impedance measurement with sparse inverse analysis," Smart Mater. Struct., vol. 27, no. 3, 2018, Art. no. 035020.
- [8] K. Deb, A. Pratap, S. Agarwal, and T. Meyarivan, "A fast and elitist multiobjective genetic algorithm: NSGA-II," *IEEE Trans. Evol. Comput.*, vol. 1, no. 2, pp. 182–197, Apr. 2002.
- [9] K. Deb and H. Jain, "An evolutionary many-objective optimization algorithm using reference-point-based nondominated sorting approach, part I: Solving problems with box constraints," *IEEE Trans. Evol. Comput.*, vol. 18, no. 4, pp. 577–601, Aug. 2014.

- [10] J. A. Duro, D. K. Saxena, K. Deb, and Q. Zhang, "Machine learning based decision support for many-objective optimization problems," *Neurocomputing*, vol. 146, pp. 30–47, Dec. 2014.
- [11] D. K. Duvenaud, "Automatic model construction with Gaussian processes," Ph.D. dissertation, Dept. Eng., Univ. Cambridge, Cambridge, U.K., 2014.
- [12] S.-E. Fang and R. Perera, "Damage identification by response surface based model updating using D-optimal design," *Mech. Syst. Signal Pro*cess., vol. 25, no. 2, pp. 717–733, 2011.
- [13] C. R. Farrar and K. Worden, "An introduction to structural health monitoring," *Philos. Trans. Roy. Soc. London A, Math. Phys. Sci.*, vol. 365, no. 1851, pp. 303–315, 2007.
- [14] H. Gao, X. Guo, H. Ouyang, and F. Han, "Crack identification of cantilever plates based on a Kriging surrogate model," ASME J. Vib. Acoust., vol. 135, no. 5, 2013, Art. no. 051012.
- [15] W. Gao, L. Huo, H. Li, and G. Song, "An embedded tubular PZT transducer based damage imaging method for two-dimensional concrete structures," *IEEE Access*, vol. 6, pp. 30100–30109, 2018.
- [16] S.-S. Jin and H.-J. Jung, "Sequential surrogate modeling for efficient finite element model updating," *Comput. Struct.*, vol. 168, pp. 30–45, May 2016.
- [17] K. Zhou, A. Hegde, P. Cao, and J. Tang, "Design optimization toward alleviating forced response variation in cyclically periodic structure using Gaussian process," J. Vib. Acoust., vol. 139, no. 1, 2017, Art. no. 011017.
- [18] K. Zhou and J. Tang, "Uncertainty quantification in structural dynamic analysis using two-level Gaussian processes and Bayesian inference," J. Sound Vib., vol. 412, pp. 95–115, Jan. 2018.
- [19] M. C. Kennedy and A. O'Hagan, "Bayesian calibration of computer models," J. Roy. Stat. Soc. B, Stat. Methodol., vol. 1, no. 3, pp. 425–464, 2001.
- [20] J. Kim and K. W. Wang, "An enhanced impedance-based damage identification method using adaptive piezoelectric circuitry," *Smart Mater. Struct.*, vol. 23, no. 9, 2014, Art. no. 095041.
- [21] M. Laumanns, L. Thiele, K. Deb, and E. Zitzler, "Combining convergence and diversity in evolutionary multiobjective optimization," *Evol. Comput.*, vol. 1, no. 3, pp. 263–282, Sep. 2002.
- [22] L. Lam and S. Y. Suen, "Application of majority voting to pattern recognition: An analysis of its behavior and performance," *IEEE Trans. Syst., Man, Cybern. A, Syst., Humans*, vol. 27, no. 5, pp. 553–568, Sep. 1997.
- [23] K. Li, K. Deb, Q. Zhang, and S. Kwong, "An evolutionary many-objective optimization algorithm based on dominance and decomposition," *IEEE Trans. Evol. Comput.*, vol. 19, no. 5, pp. 694–716, Oct. 2015.
- [24] J. Li and S. Law, "Substructural response reconstruction in wavelet domain," J. Appl. Mech., vol. 78, no. 4, 2011, Art. no. 041010.
- [25] R. M. Neal, "MCMC using Hamiltonian dynamics," in *Handbook of Markov Chain Monte Carlo*, vol. 2, no. 11. Boca Raton, FL, USA: CRC Press, 2011.
- [26] S. Park, J.-J. Lee, C.-B. Yun, and D. J. Inman, "Electro-mechanical impedance-based wireless structural health monitoring using PCA-data compression and k-means clustering algorithms," J. Intell. Mater. Syst. Struct., vol. 19, no. 4, pp. 509–520, 2008.
- [27] R. Perera, S.-E. Fang, and A. Ruiz, "Application of particle swarm optimization and genetic algorithms to multiobjective damage identification inverse problems with modelling errors," *Meccanica*, vol. 45, no. 5, pp. 723–734, 2010.
- [28] W.-X. Ren and H.-B. Chen, "Finite element model updating in structural dynamics by using the response surface method," *Eng. Struct.*, vol. 32, no. 8, pp. 2455–2465, 2010.
- [29] C. E. Rasmussen and K. I. Williams, Gaussian Processes for Machine Learning, vol. 1. Cambridge, MA, USA: MIT Press, 2006.
- [30] Q. Shuai, K. Zhou, S. Zhou, and J. Tang, "Fault identification using piezoelectric impedance measurement and model-based intelligent inference with pre-screening," *Smart Mater. Struct.*, vol. 26, no. 4, 2017, Art. no. 045007.
- [31] A. D. Taylor and A. M. Pacelli, Mathematics and Politics: Strategy, Voting, Power and Proof. New York, NY, USA: Springer, 2008.
- [32] H.-P. Wan and W.-X. Ren, "A residual-based Gaussian process model framework for finite element model updating," *Comput. Struct.*, vol. 156, pp. 149–159, Aug. 2015.
- [33] K.-W. Wang and J. Tang, Adaptive Structural Systems with Piezoelectric Transducer Circuitry. New York, NY, USA: Springer, 2008.
- [34] X. Wang and J. Tang, "Damage detection using piezoelectric admittance approach with inductive circuitry," *J. Intell. Mater. Syst. Struct.*, vol. 21, no. 7, pp. 667–676, 2010.

- [35] Z. Wang, J. Ma, and L. Zhang, "State-of-health estimation for lithiumion batteries based on the multi-Island genetic algorithm and the Gaussian process regression," *IEEE Access*, vol. 5, pp. 21286–21295, 2017.
- [36] Z. Xia and J. Tang, "Characterization of dynamic response of structures with uncertainty by using Gaussian processes," ASME J. Vib. Acoust., vol. 135, no. 5, 2013, Art. no. 051006.
- [37] X. Yang, X. Guo, H. Ouyang, and D. Li, "A Kriging model based finite element model updating method for damage detection," *Appl. Sci.*, vol. 7, no. 10, p. 1039, 2017.
- [38] W. Zhou and L. Zuo, "Sensitivity-enhanced admittance-based structure health monitoring using a higher-order resonant circuit," *Smart Mater. Struct.*, vol. 21, no. 10, 2012, Art. no. 105023.
- [39] E. Zitzler, "Evolutionary algorithms for multiobjective optimization: Methods and applications," Ph.D. dissertation, Dept. Comput. Eng. Netw. Lab., Swiss Federal Inst. Technol., Zürich, Switzerland, 1999.
- [40] Q. Zhang and H. Li, "MOEA/D: A multiobjective evolutionary algorithm based on decomposition," *IEEE Trans. Evol. Comput.*, vol. 1, no. 6, pp. 712–731, Dec. 2007.
- [41] S. Chakraborty and A. Sen, "Adaptive response surface based efficient finite element model updating," *Finite Elements Anal. Des.*, vol. 80, pp. 33–40, 2014.
- [42] M. L. Stein, Interpolation of Spatial Data: Some Theory for Kriging. New York, NY, USA: Springer, 2012.



**PEI CAO** received the B.S. degree in automation from Northwestern Polytechnical University, Xi'an, China, in 2011. He is currently pursuing the Ph.D. degree in mechanical engineering with the University of Connecticut, Storrs, USA. His research interests include global optimization, dynamic programming, statistical inference, layout design, and machine learning.



**QI SHUAI** received the B.S. and M.S. degrees in mechanical engineering from Chongqing University, Chongqing, China, in 2008 and 2011, respectively, and the Ph.D. degree in mechanical engineering from the University of Connecticut, Storrs, USA, in 2017. After graduation, he joined Chongqing University, as an Assistant Professor, where he focuses on product development and experimental data analysis as well as product performance prediction and analytical dynamic analysis.



JIONG TANG (M'09) received the B.S. and M.S. degrees in applied mechanics from Fudan University, China, in 1989 and 1992, respectively, and the Ph.D. degree in mechanical engineering from Pennsylvania State University, USA, in 2001. He was a Mechanical Engineer with the GE Global Research Center, from 2001 to 2002. He then joined the Mechanical Engineering Department, University of Connecticut, where he is currently a Professor and the Director of the Dynamics,

Sensing, and Controls Laboratory. His research interests include structural dynamics and system dynamics, control, and sensing and monitoring. He has served as an Associate Editor for the IEEE Transactions on Instrumentation and Measurement, from 2009 to 2012. He also served as an Associate Editor for the *Journal of Vibration and Acoustics* (ASME), and *Journal of Dynamic Systems, Measurement, and Control* (ASME). He currently serves as an Associate Editor for the IEEE/ASME Transactions on Mechatronics.

. . .

94496